Energy 69 (2014) 728–741

Contents lists available at ScienceDirect

Energy

journal homepage: www.elsevier.com/locate/energy

Multi-channel heat exchanger-reactor using arborescent distributors: A characterization study of fluid distribution, heat exchange performance and exothermic reaction

Xiaofeng Guo [a,b,1], Yilin Fan [a], Lingai Luo [a,*]

[a] Laboratoire de Thermocinétique, UMR CNRS 6607, Polytech'Nantes – Université de Nantes, La Chantrerie, Rue Christian Pauc, BP 50609, 44306 Nantes Cedex 03, France

[b] Laboratoire Optimisation de la Conception et Ingénierie de l'Environnement – LOCIE CNRS UMR5271, Université de Savoie, Campus Scientifique, Savoie Technolac, 73376 Le Bourget du Lac Cedex, France

ARTICLE INFO

Article history:
Received 3 December 2013
Received in revised form
14 March 2014
Accepted 16 March 2014
Available online 14 April 2014

Keywords:
Multi-channel
Multifunctional heat exchanger-reactor
Arborescent structure
Fluid distribution
Heat exchange performance
Thermal control

ABSTRACT

A multi-functional heat exchanger-reactor comprising arborescent (tree-like) distributors and collector, 16 mini-channels in parallel and T-mixers is introduced in this paper. Flow distribution property, pressure drop and heat exchange performance of proposed heat exchanger-reactor are tested and discussed. Firstly, flow distribution uniformity is characterized by CFD simulation and then qualitatively confirmed by visualization experiment. Results show that for total flowrates ranging from 5 mL s^{-1} to 20 mL s^{-1}, good distribution uniformity is obtained, with maximum flowrate deviation less than 10%. Then, experiments of heat exchange between hot and cold water are carried out. High values of overall heat transfer coefficient ranging from 2000 to 5000 W m^{-2} °C^{-1} are obtained under our working conditions. The volumetric heat exchange capability (UA/V) is found to be around 200 kW m^{-3} °C^{-1}, showing a high heat exchange capability with compact design. The roles of end-effect and non-established flow are discussed and are supposed to be responsible for efficient heat transfer. Finally a typical fast exothermic reaction, neutralization between acid and basic solutions, is carried out to test the thermal control capability of the studied heat exchanger-reactor. Results indicate that isothermal condition could be realized by circulating appropriate flowrate of coolant through the heat exchanger.

The design of heat exchanger-reactor with arborescent distributor and collector makes possible the application of multi-channel systems. This paper introduces systematically the successful integration of heat exchanger-reactor and its performance evaluation.

1. Introduction

Heat exchanger usually appears in typical energy systems relating energy production, transportation, storage and conversions [1,2]. These systems are not intended merely to heat exchange but involve other processes and functions. Integration of heat exchanger with several system components, i.e. multifunctional devices, may be interesting in that energy consumption might be reduced and the system performance may be raised.

An example in the chemical engineering would be the heat exchanger-reactor integration. According to a study of ADEME (French Agency of Environment and Energy Management), energy consumption in a chemical plant contributes in average 61.7% of the final price of products [3]. Among different energy consumptions, thermal energy is the main source that guarantees proper control and management of process conditions. Usually this thermal condition is provided by circulating utility fluid. In low temperature conditions liquids are used as utility fluid while in higher temperature conditions (>100 °C) like in petrochemical processing, pressurised steam is served as the medium [4]. A better temperature control with reduced temperature difference between the utility fluid and process fluid is usually beneficial, regarding both process integration improvement [4] and exergy efficiency [5]. In particular, as studied by Cheng [6], entropy resistance should be minimized in

* Corresponding author. Tel.: +33 2 40 68 31 67; fax: +33 2 40 68 31 41.
E-mail addresses: xiaofeng.guo@esiee.fr (X. Guo), yilin.fan@univ-nantes.fr (Y. Fan), lingai.luo@univ-nantes.fr (L. Luo).
[1] Present address: ESIEE Paris, Department SEN, Cité Descartes – 2 bd Blaise Pascal BP 99, 93162 Noisy Le Grand Cedex, France.

http://dx.doi.org/10.1016/j.energy.2014.03.069
0360-5442/

Nomenclature

Notations

A	heat transfer surface area (m^2)
C	concentration (mol L^{-1})
c_p	fluid heat capacity (J g^{-1} °C^{-1})
d_i	tube internal diameter (m)
d_o	tube external diameter (m)
D_{ch}	flowrate deviation (%), defined by Eq. (1)
F	correction factor
f_{ch}	mass flowrate in a channel (kg s^{-1})
f_{av}	calculated average mass flow in each channel (kg s^{-1})
h	convective heat exchange coefficient (W m^{-2} °C^{-1})
ΔH	standard molar enthalpy of formation (kJ mol^{-1})
ΔH_r	reaction enthalpy (kJ mol^{-1})
$\dot{m}$	total mass flowrate (kg s^{-1})
Nu	Nusselt number
Pr	Prandtl number of fluid
Q	volume flowrate (mL s^{-1})
Re	Reynolds number
Φ	heat exchange rate (W)
λ	thermal conductivity of fluid (W m^{-1} °C^{-1})
λ_{cc}	thermal conductivity of Cobalt Chrome (W m^{-1} °C^{-1})
T	temperature (°C)
U	overall heat exchange coefficient (W m^{-2} °C^{-1})
V	total volume of reactor (m^3)
ΔP	pressure loss (bar)
ρ	density (kg m^{-3})

Indices

h, c	hot or cold side
i, o	inlet or outlet of fluid
effective	effective transfer area considering end effects
process	process fluid, tube-side fluid
utility	utility fluid, shell-side heat exchanging fluid
w, f	wall or fluid

order to reach high heat exchange performance. One alternative is to reduce the temperature difference between two fluids.

Besides energy efficiency, reaction quality is another aspect that may benefit from integrated design. Temperature control for exothermic or endothermic reactions has vital influence on the final process yield. However, many conventional equipment such as stirred tank reactors that incorporate heat transfer in the process, i.e. by using double jacket, external or internal coil, cannot supply or remove heat as efficiently as it is required by reaction. A compact device that combines reaction and heat transfer into a single equipment, i.e. using for instance a heat exchanger as a chemical reactor, the so-called *multifunctional heat exchanger*, could be an appropriate solution.

1.1. Micro/mini flow system

One of the methods to achieve compact, multifunctional exchangers is through the use of micro/mini scale channels (the so-called microfluidic equipment), as reviewed by Brandner et al. [7] and by Fan and Luo [8]. Advantages of microfluidic devices include high surface-to-volume ratio (named specific area, A/V, interfacial area in the case of mass transfer, and transfer surface area in the case of heat transfer), and improved safety. For example, a basic parameter to describe the "compactness" is the volumetric heat exchange capability, calculated as the product of overall heat exchange coefficient and specific area (UA/V). For micro channel heat exchangers this parameter is higher by several orders of magnitude than that of conventional devices. Moreover, safety and security in chemical and energy processes can be improved. Using microfluidic system, continuous process is easier to be realized with online monitoring. Reaction run-aways could be avoided by effective thermal management too.

However, to obtain a comparable productivity with that of conventional equipment, it is inevitable to put together a number of micro/mini-channels in parallel instead of mono-channel devices. This so-called *numbering-up* process is the key issue for industrial applications of microfluidic devices in large scale [9]. In that case, problem of fluid distribution from a single inlet port to an array of parallel micro-channels, and the reverse for collection, may have important influence on the global performance of multichannel equipment. Fluid maldistribution often deteriorates global performance of such devices. According to a study by Lalot et al. [10], a loss of heat exchange effectiveness could be up to 25% with the presence of maldistribution. Another particularity, in the case of chemical reaction, varied proportion of reactants caused by maldistribution may result in totally different products. As a result, distributing and collecting flow structures in a multichannel system need to be treated carefully.

1.2. Arborescent structure application

The arborescent structure, also known as tree-like structure, is a natural way of obtaining identical flow paths from "root" to "branches" or vice versa. The former case is the function of fluid distributor while the latter one is fluid collector. A general guideline on multi-scale design of fluid distributors can be found in Ref. [11], regarding both pressure drop and distribution character. Arborescent geometry is a "natural" option, which exhibits significant advantages in the numbering-up process in order to augment the productivity.

The fabrication difficulty usually prohibits the wide application of arborescent structures in industries because traditional fabrication methods are often constrained by size or complexity. However, the fast development of modern fabrication methods makes it more than possible but efficient to realize some non-conventional structures. While with 3D printing or other rapid prototyping methods like SLA (Stereo-lithography Apparatus) and DMLS (Direct Metal Laser Sintering), complex features could be rapidly realized without much intervention from technical personnel. The advancement of machinery technology also pushes the application of multi-scale, miniature arborescent structures.

The internal numbering-up of multiple channels using tree-like structures has been studied in our previous publications [12–17]. Firstly, the general philosophy of arborescent component and its scaling principles are introduced by Luo et al. [13]. Applications of similar structures in heat exchangers [12–14], mixer [15] and reactor [16,17] are successively reported. In most of these applications, arborescent structures are verified to be advantageous on global system performance compared with conventional fluid distributors and collectors.

As a continuation of the previous study on mixing performance by Guo et al. [17] over a multi-channel heat exchanger-reactor, this paper aims at giving a comprehensive investigation on its flow distribution and heat exchange performances. Firstly, the geometry of the heat exchanger-reactor is briefly described. Then, detailed experimental and simulation regarding flow uniformity, pressure

drop and heat exchange characteristics are discussed. Finally, a typical exothermic neutralisation reaction is used to verify the thermal control capability of studied heat exchanger-reactor.

2. Multifunctional heat exchanger with arborescent structure

2.1. Multifunctional concept

Illustrated in Fig. 1 is the proposed multifunctional heat exchanger. An arborescent structure, shown in Fig. 1a, is used as both distributor and collector. 16 Sub-channels are connected and reunited at one single port, which is the inlet for the case of distributor and the outlet for the case of collector. Fluid in each branch has identical flow-path to reach the final outlet port. Distribution of fluid is expected to be uniform in this way. For simplicity and compactness reasons, identical channel sizes are used. No scaling law such as constructal rule is applied.

Applying the above structure as two distributors and a collector, an integrated flow structure is proposed. The first reactant is fed from inlet port (Inlet I in Fig. 1b, highest scale of distributor) to 16 outlet ports (lowest scale) and the fluid is evenly distributed. Using the same principle, the second reactant is also evenly supplied from Inlet II. The two fluids firstly arrive in a counter-current manner and contact with each other at 16 T-mixers and then enter the stack of parallel channels where chemical reaction happens. Final product of reaction is collected by the collection part. By circulating utility fluid around the parallel channels to remove or provide the reaction heat, we can control the reaction conditions which in turn determine the overall reaction yield.

A 2D sketch is shown in Fig. 1b to better illustrate the multifunction character. Two inlets of solutions (shown in orange colour) and their mixing through T-mixers are shown in upper side of the figure. Reaction tubes are immersed in utility fluid (shown in blue), which is supposed to provide (iso)thermal condition to reaction. Final reaction products are collected to the outlet port shown in lower part of the figure. Only 4 tubes can be seen in this 2-dimensional figure while in reality there are 16 channels in parallel at 3 dimensions. (For interpretation of the references to colour in this paragraph, the reader is referred to the web version of this article.)

The example shown in Fig. 1 has 16 channels in parallel and current scale of arborescent structure is 4 ($2^4 = 16$). We can easily imagine more channels such as 32, 64 or 128 by using higher scale tree-like structures.

2.2. Prototype fabrication, quality inspection and dimensions

With the concept shown in Fig. 1b, two different sizes of heat exchanger-reactors are fabricated. One has a channel diameter of 1 mm while the other with doubled size. For clarity, they are named as M1 (diameter: 1 mm, length of straight channel: 15 mm) and M2 (diameter: 2 mm, length of straight channel: 50 mm), respectively. Dimensional details of the arborescent distributor can be found in Ref. [17].

Both the two prototypes are fabricated using rapid prototyping. DMLS is used to fabricate the metal compact exchanger-reactor M1. The fabrication concerns fritting small sized metal powders in a selective manner by laser beams. SLA is used during the fabrication of M2. In this process, photopolymer is cured selectively at the local focus of ultraviolet laser. Both processes require repeated laser scanning layer by layer until the final layer is completed. Powder used for M1 is Cobalt-Chrome, and the polymer used for M2 is transparent resin.

Metal-made M1 has been used for heat exchange test, whereas with the transparent feature of M2, we were able to visualize the internal flow using fast camera and optical tracers. Photo of prototype M2 can be found in Fig. 1d.

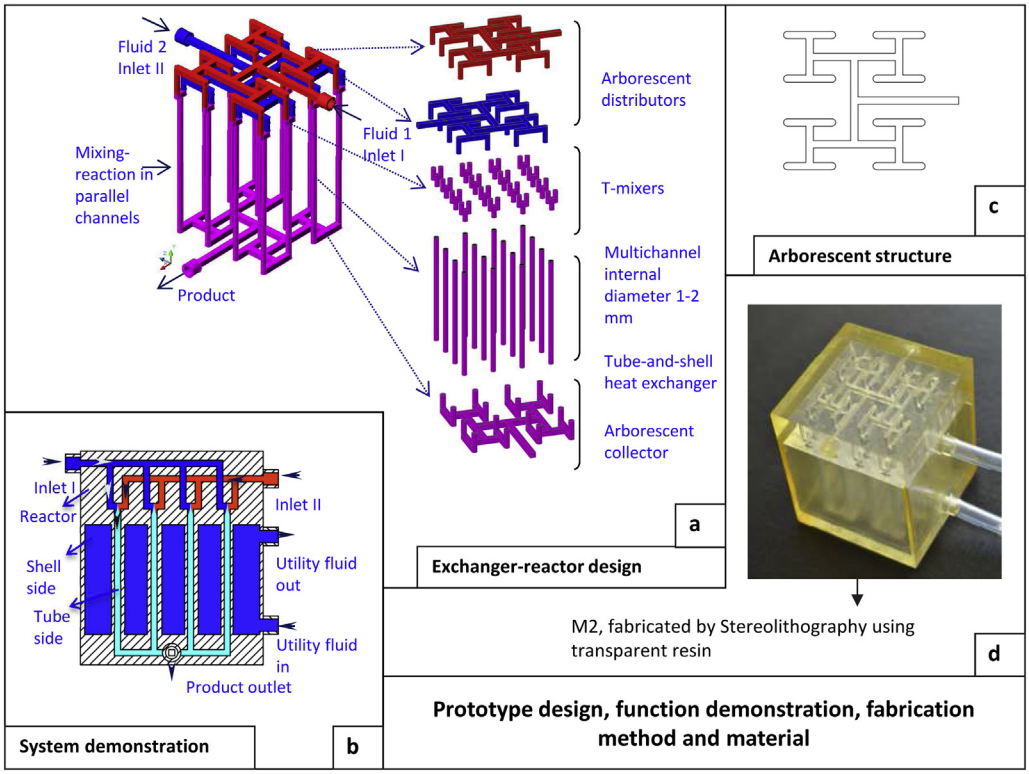

Fig. 1. Heat exchanger-reactor with arborescent structure – design, structure and prototype.

Table 1
Geometry parameters of multichannel heat exchanger-reactor M1.

Parameter	Value
Total channel number after mixing	16
Channel inner diameter (mm)	1
Channel exterior diameter (mm)	2
Pitch of channels (mm)	6
Channel length (mm)	15
Channel length for heat exchange (mm)	12.5
Tube-and-shell heat exchange surface (m^2)	1.26×10^{-3}
Effective heat exchange surface[a] (m^2)	2.72×10^{-3}
Outside total volume (m^3)	2.25×10^{-5}
Specific heat transfer area ($m^2\ m^{-3}$)	56
Effective specific heat transfer area ($m^2\ m^{-3}$)	121

[a] Effective heat exchange surface, including tube-and-shell exchange surface (using outside dimension of channel) and that of two end-effect exchange surface areas.

Some useful geometry parameters of M1 are given in Table 1. Specific transfer area (transfer area density) is calculated as: $A/V = 56\ m^2\ m^{-3}$, where V is the total exchanger volume including both distributor and collector, while for heat transfer area (A) only the exterior surface area of 16 parallel channels is considered. Effective specific transfer area ($A_{effective}/V$) is also calculated, which includes both the shell-and-tube surface area and that of the surface at two ends of utility fluid chamber. The value of effective specific transfer area is $A_{effective}/V = 121\ m^2\ m^{-3}$. The effective transfer area will be discussed in the Heat exchange study section. For M2 the basic geometrical dimensions are doubled accordingly.

Internal structure details of the metal-made M2 are inspected with 3-dimensional micro-tomography analysis. Shown in Fig. 2 are top and lateral views of cutting sections of M1. Quality of DMLS prototyping is satisfactory in that both arborescent structure and parallel channels are in agreement with the geometrical design.

3. Flow distribution uniformity and pressure drop

3.1. Simulation of flow distribution by CFD (Computational Fluid Dynamics)

We present here some numerical results on flow distribution uniformity of the heat exchanger-reactor under laminar flow (average *Re* inside channels being lower than 2300). Resin-made, transparent M2 is taken as the geometry.

3.1.1. Simulation parameters

The overall model and simulation are realised using different modules of ANSYS Workbench 12.1. The internal fluid body illustrated in Fig. 1 is created geometrically and prepared for meshing. ANSYS mesh tool for CFD analysis is used to obtain the tetra patch conforming mesh. Near the wall, an inflation of 5 layers is created for better presenting the mechanism of near wall flow transition under laminar flow.

Simulations use Fluent to solve conservation equations of mass and momentum. Different models are used to solve the Navier–Stokes equation, depending on the flow regime. For low throughputs under 5 mL s^{-1}, laminar flow model is used. Whilst for higher flowrates, several scales in distributor and collector structure are under turbulent flow regime, we thus use k–ε RNG (Re-Normalisation Group) segregated turbulent solver. For the pressure–velocity coupling, standard SIMPLE method is employed. Finally regarding discretization, standard method is chosen for pressure and second-order upwind differentiation for momentum.

Boundary conditions are setup as velocity inlet for both inlet I and II. We use identical inlet velocities for both inlet I and II. Outlet is set to be static pressure boundary, with the pressure value being the same as ambient pressure. All the internal faces are defined as non-slip boundaries. Pure water at constant temperature of 27 °C (300 K) is chosen as the working fluid.

The solution is considered to be converged when (i) the mass flowrate at each channel and the inlet static pressure are constant from one iteration to the next (less than 0.5% variation) and (ii) the normalized residuals for velocities and continuity are lower than the order of magnitude of 10^{-6}. For turbulent flow simulation using k–ε equation, residuals of the turbulent kinetic energy k and turbulent dissipation ε are considered to be converged once they are lower than 10^{-6}.

Different sizes of the mesh are tested as a grid independence study. By adjusting the overall element number among 1.3 million, 1.7 million and 2.2 million, the difference between each calculated results (inlet pressure) are 5.7% and 1.8%. After considering both calculation time and the precision of results, an overall element number of 1.7 million is chosen.

3.1.2. Contour of flow

Uniformity of flow distribution could be reflected qualitatively by the contours of velocity magnitude, as shown in Fig. 3. Contours are obtained by cutting sectional surfaces through the two distributors and the collector in CFD post-processing. Shown in the figure is the case of overall throughput being 2.4 mL s^{-1} (144 mL min^{-1}), and Reynolds number being 95 inside channels (after T-mixing). Maximum Reynolds number in the whole flow structure is 1195, which happens in the final scale of collector (near outlet).

Fluid inside of the arborescent structures shows good bifurcation at each branch according to the contour. For the case of distributor, inlet streams separate in a similar manner to two opposite directions, where fluid continues to flow and redevelop until it separates again at the next branch. The same character is found for the case of collector, where streams are visibly identical

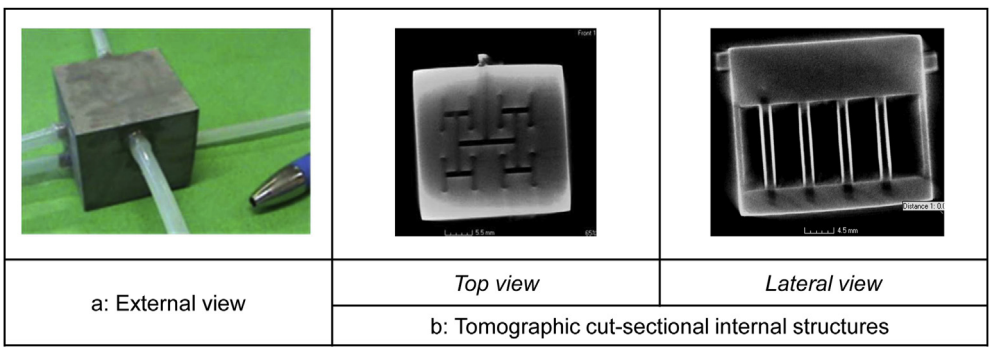

Fig. 2. Photo of M1 made by DMLS and its fault detection using 3D tomographic analysis.

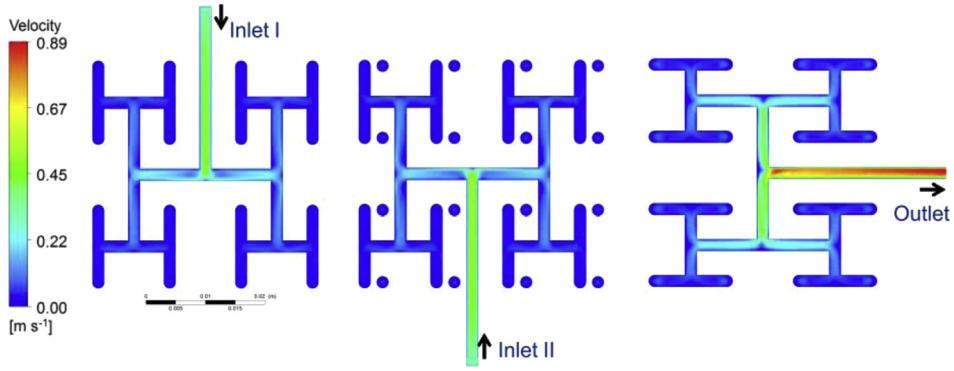

Fig. 3. Field of velocity in inlet distributor I (left), inlet distributor II (middle) and outlet collector (right), with $Re = 95$ in parallel straight channels, case of M2.

before each merging. Flow pattern after each bifurcation tends to be the same, and this shows that the designed arborescent structure is effective in distributing fluid.

Inertial force could result in uneven bifurcation, which cannot be shown qualitatively from the flow pattern. Velocity doubles and so as the Reynolds number after each merging. For the case shown in the figure, the maximum Reynolds number is lower than 2300. Flow in the whole structure is kept under laminar regime. A relatively long distance [18] is needed for the streams to be fully developed in this case. With a short developing channel length compared with the sectional dimension, flow is not fully developed and inertial force may result in flow maldistribution. A quantitative study is thus done and presented in next section.

3.1.3. Quantitative flow distribution evaluation

To better explain the distribution uniformity in a quantitative way, we define a relative channel flowrate deviation (D_{ch}) as:

$$D_{ch} = \left(\frac{f_{ch}}{f_{av}} - 1\right) \times 100\% \quad (1)$$

where f_{ch} is the mass flowrate in a channel, kg s^{-1}, and f_{av} stands for the calculated average mass flowrate considering all 16 channels.

According to the definition, fluid distribution is uniform when $D_{ch} = 0$; big values of D_{ch} mean higher departure of the flowrate in a channel with respect to the ideal uniform case. Results of D_{ch} for different throughputs (5, 14 and 20 mL s^{-1}) are shown in Fig. 4. Reynolds numbers in channels after mixing are also shown accordingly.

From Fig. 4, a general maldistribution under 10% is found for the three throughputs studied. Maximum deviation D_{ch} is calculated to be 2.33%, 5.29% and 8.68%, corresponding to a throughput of 5, 14 and 20 mL s^{-1}, respectively. With the increase of Reynolds number, the flow distribution becomes less uniform. This is possibly due to the bigger the Reynolds number (under laminar flow), the longer a channel is needed for the flow to redevelop after each bifurcation. In other words, at a certain position of channel, the sectional flow profile is less symmetrical under high *Re* number conditions.

The asymmetrical sectional flow character results in non-uniform distribution at flow bifurcation. This could be verified by examining the cross-sectional velocity field at different positions of distributor, as shown in Fig. 5. Contours of velocity and vectors firstly reflect non-uniform velocity field after the first bifurcation. Then the velocity field becomes more symmetrical as flow becomes further developed along the flow direction. Finally another splitting of fluid happens at the next bifurcation after which flow becomes asymmetrical again. In the end, after several splits in the distributor, the final flowrate uniformity among channels might be influenced. We then conclude that whether velocity profile is redeveloped to be symmetrical between two successive bifurcations determines the final distribution uniformity.

3.2. Visualization of flow distribution

Fluid distribution is visualized experimentally using fast camera and ink injection to the transparent prototype M2. Fast camera (PHOTRON, FASTCAM-PCI R2) is used to capture photos of distributing structure at different time instants. Successive photos with a time interval of 1/15 s are presented. Shown in Fig. 6 is the illustration of visualized ink invasion to the arborescent distributor.

Similar to the CFD contour results, these pictures qualitatively illustrate the evolution of the ink injection and thus the distribution uniformity. Injected ink is evenly distributed into 2 divisions (at 0 s), then to 4 divisions (at 1/15 s) and finally into 16 channels at 1/

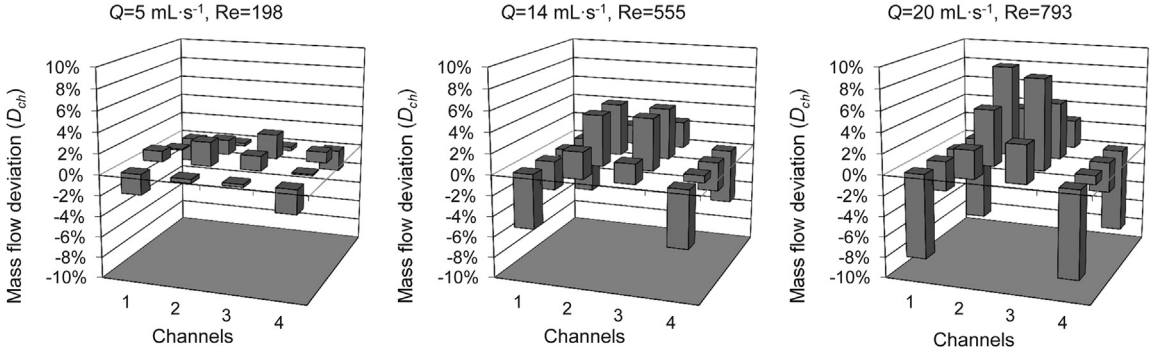

Fig. 4. Maldistribution among channels with throughput *Q* and Reynolds number inside channels *Re*. Result of CFD analysis, case of M2.

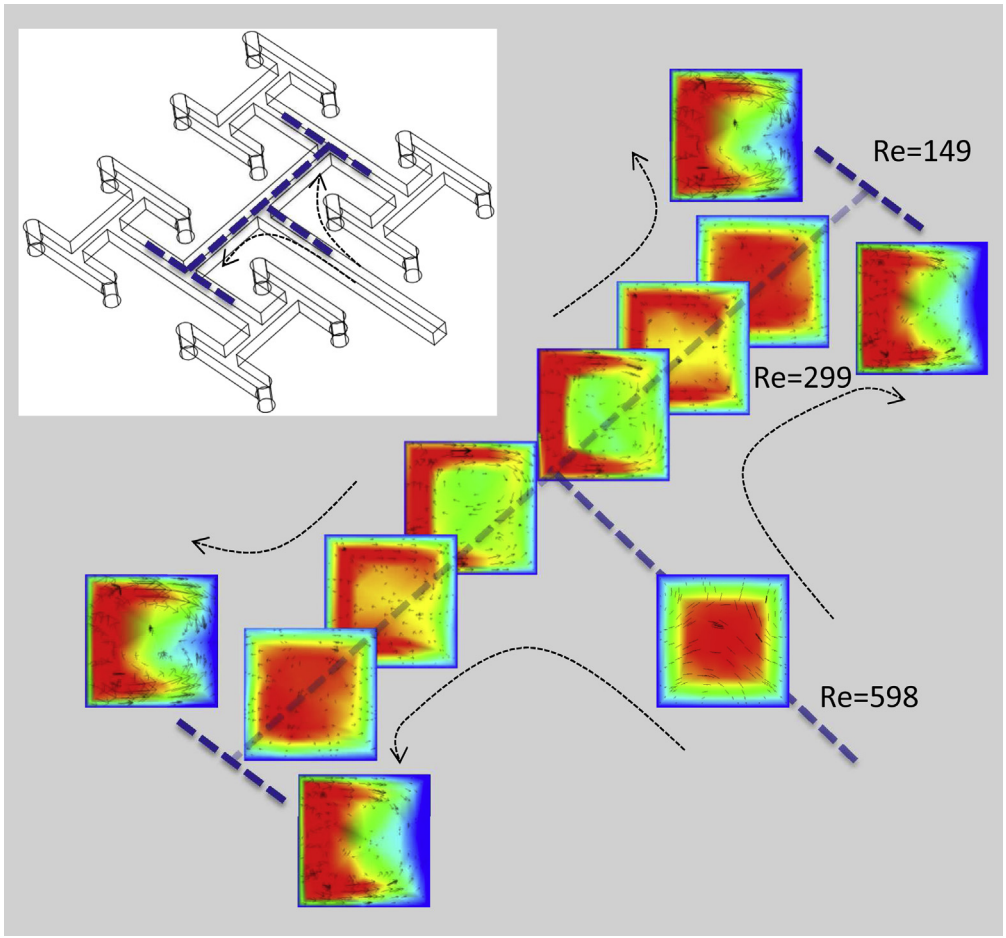

Fig. 5. Inertial force influence on flow distribution, result of CFD under throughput of 2.4 mL s^{-1} (144 mL min^{-1}).

5 s. Generally no obvious concentration difference is found at each bifurcation. The visualisation result may be considered as a rough validation to the CFD results.

3.3. Total pressure drop characterization

Pressure drops for prototype M1 are measured using pressure sensor (SEN-3247 membrane sensor, 0–1 bar, ±0.1% precision, KOBOLD Messring GmbH). Measuring point is placed close to the reactor inlet to minimize the influence of tubing. At the outlet liquid runs out directly to a drain. Pressure drops at various flowrates (flowrate is measured by weighing method using a digital balance and a stopwatch) are studied. The highest throughput is limited by a maximum pressure drop of 1 bar.

Fig. 7 shows that for a maximum pressure drop of 1 bar, throughput (production flowrate) of M1 could be up to 8.3 mL s^{-1} (about 500 mL min^{-1}), the flowrate at utility side could be as high as 18.3 mL s^{-1} (about 1100 mL min^{-1}). The utility fluid side shows lower pressure loss character due to its simple structure (less friction of tube flow). Globally, the obtained flowrate with pressure drop under 1 bar is high compared with that of most microfluidic devices [19]. More results regarding pressure loss, dissipation rate characters could be found in our earlier work [17].

3.4. Discussions on hydrodynamic performance

The obtained results show good flow distribution uniformity and relatively low total pressure drop of the studied multichannel heat exchanger-reactor, by employing arborescent fluid distributors and collector. However, it should be noted that arborescent structure used in the current study has identical channel sizes, so that it is rather a "non-optimized" tree-like concept. The main difference between the present design and the constructal optimized design is that *no scaling relations were applied to the tree-like structure*. This is surely not the "*best design*" in terms of pressure drop. As discussed in our earlier study [17], the pressure loss no longer follows that of laminar Hagen–Poiseuille law but higher. However, this choice was made based on two main considerations:

Firstly, constructal optimized design with different channels sizes may affect the compactness of the component because higher pitches between tubes are required. If we consider that two such structures should be stacked one above another for two different fluids to be mixed, more spaces are thus needed. Secondly, the constructal optimization is based on the assumption of even flow distribution among all parallel channels owing to the geometrically symmetrical structure [20]. In reality, this is not always the case, as have been shown in Fig. 5. In order to guarantee an equal bifurcation, the distance between two bifurcations should be long enough so that a symmetrical velocity profile can be developed. Larger channel size after applying constructal scaling law results in smaller length-to-diameter ratio, which has a negative effect on the redevelopment of symmetrical velocity profile. As a result, the overall flow distribution may become less uniform.

To conclude, the use of "non-optimized" design instead of "constructal optimized" structure as fluid distributor/collector is to gain the compactness on one hand, and to address more on the

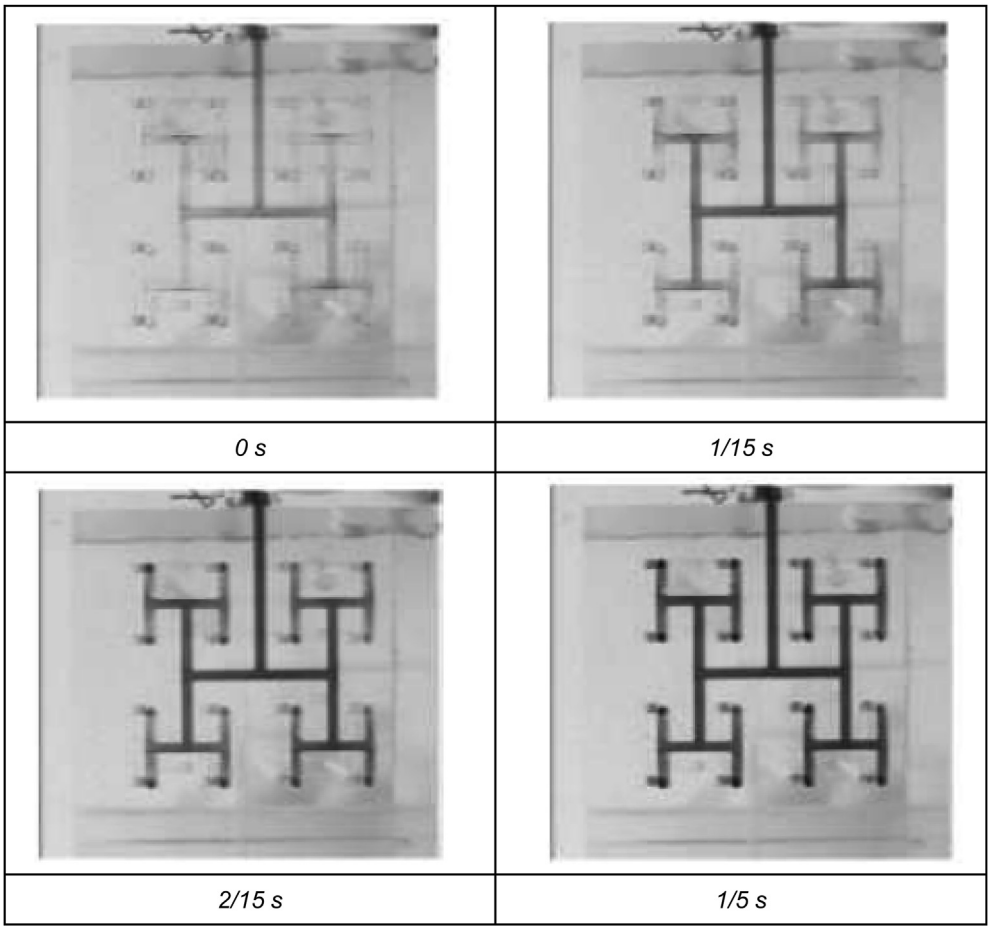

Fig. 6. Visualization of fluid distribution by fast camera and ink injection. At the inlet of distributor $Re = 3320$, corresponding flowrate to each inlet $Q = 6.7$ mL s^{-1} (400 mL min^{-1}), case of M2.

criterion of uniform flow distribution on the other. This consideration is at the cost of a higher total pressure drop, but within an acceptable limit. To further reduce the total pressure drop while keeping a uniform flow distribution, advanced numerical algorithm based on heuristic optimality criteria was proposed and tested [21,22].

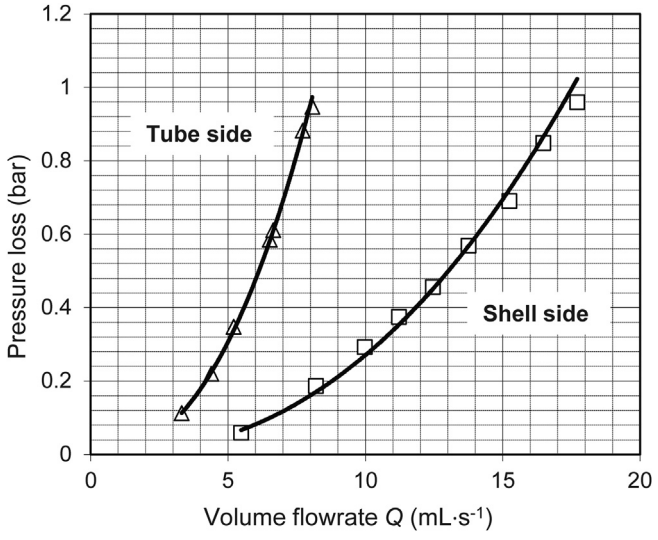

Fig. 7. Pressure drop character at process fluid (tube-side) and utility fluid (shell-side), case of M1.

The use of arborescent distributors and collector will also improve the heat transfer performance, as shown in following sections concerning the "end-effect".

4. Heat exchange performance evaluation

Heat exchange experiments have been carried out to the designed multi-channel heat exchanger-reactor. Here the heat exchange property of the metal-made exchanger M1 is tested, using hot and cold water as working fluid. During the test, several different flowrates are studied, with flow inside parallel channels being always under laminar regime.

4.1. Experiment and data reduction

4.1.1. Experimental setup

The experimental setup is composed of two loops: process fluid loop and utility fluid loop. Process fluid is pumped inside heat exchanger-reactor from one of its inlets and fluid flows successively through distributor, channels (tube side) and collectors. Utility fluid is taken as cooling or heating loop, and it flows through the shell side (outside of channels) of heat exchanger. Two adjustable pumps (gear pump, max. 2000 mL min^{-1}, flowrate adjustable with input voltage, Diener Precision Pump Ltd.) are used to circulate the two loops of fluid. A circulation thermostat (LAUDA E200, 0–200 °C range, using R134a as refrigerant, 2.5 kW, LAUDA Dr. R. Wobser Gmbh & Co. KG., Germany) is used to control the temperature of utility fluid. Thermalcouples (K-type, together with a platinum RTD

(Resistance Thermal Detector) compensation to the cold junction, overall precision of thermocouple within ±0.5 °C) are placed in the loop for temperature measurements. A data acquisition centre (Agilent 34972A, Agilent Technologies) records temperatures automatically. Process loop through channels is circulated with tap water, whose initial temperature is stable (ranging from 24.5 °C to 25.5 °C) during the test. The heat transfer (utility) fluid circulates through the thermostat to obtain a stable high/low temperature. Mass flow of the each fluid is related with the rotational speed of gear pump, whose motor frequency output is monitored.

Schema of the experimental setup is shown in Fig. 8. Globally the heat exchanger and its connecting tubes are insulated from ambient during the experiments. Thermalcouples are placed inside the connecting tubes as close to inlet/outlet ports as possible. Influence of ambient temperature is minimized in this way.

Experiment data are captured when all physical parameters are stable. Time needed for the mini-exchanger to reach steady state is rather limited, usually in about several seconds. Tests are repeated several times under the same conditions to check the repeatability until consistent results are obtained.

Two series of tests are implemented so as to represent both cases of endothermic and exothermic reaction application. As a heat exchange test for endothermic reaction (heating test), inlet of utility fluid is controlled by the thermostat at 60 °C and that of reactant (process fluid) inlet is 25 °C. For the case of exothermic reaction usage, cooling test is done by controlling the inlet of utility fluid at 5 °C and that of process fluid at 25 °C.

Flowrates of both tube and shell side are varied during the experiment. Shell-side mass flowrates are varied from 2.60 g s^{-1} to 9.17 g s^{-1} and corresponding Reynolds numbers range from 400 to 1600 (calculated by KERN correlation [23]). Tube-side Reynolds numbers of 275 and 568 are tested, with corresponding mass throughput being 2.89 g s^{-1} and 5.97 g s^{-1}, respectively.

4.1.2. Heat exchange rate

Calculation of heat exchange rate based on measured flowrate and temperature difference could be done using the equation:

$$\Phi = \dot{m} c_p \Delta T \tag{2}$$

where Φ is the heat exchange rate, W; $\dot{m}$ the mass flowrate of fluid, kg s^{-1}; c_p the heat capacity of fluid, here constant value of water is used, 4.1813 J g^{-1} °C^{-1}; and ΔT is the temperature difference between the inlet and outlet, °C.

Heat loss during the test can be calculated by the difference between the heat exchange rate of utility fluid and that of process fluid:

$$\Phi_{loss} = \left| \Phi_{utility} - \Phi_{process} \right| \tag{3}$$

Here the indices utility and process stand for the utility side (shell) and process fluid side (tube), respectively. During the test, a heat loss within 10% is found, meaning that a portion of heat was released to the ambient despite all insulating measures taken. The real heat exchange rate is estimated by the average of the two values (say, between $\Phi_{utility}$ and $\Phi_{process}$), and is then used to calculate the overall heat transfer coefficient.

4.1.3. Overall heat exchange coefficient

Overall heat exchange coefficient is calculated with measured heat exchange rate, transfer surface area (outside surface of channels) and mean temperature difference:

$$U_{experiment} = \frac{\Phi}{A_o F \Delta T_m} \tag{4}$$

In Equation (4), A_o stands for the outside surface area of channels, m^2; F is the correction factor for using the LMTD (logarithmic mean temperature difference) method. For a single tube pass "shell and tube heat exchanger", the value of F is proposed to be equal to 1 for estimation [24].

The log-mean temperature difference is calculated by equation:

$$\begin{aligned} \Delta T_m &= \frac{\Delta T_2 - \Delta T_1}{\ln(\Delta T_2 / \Delta T_1)} \\ \Delta T_1 &= T_{h,i} - T_{c,o} \\ \Delta T_2 &= T_{h,o} - T_{c,i} \end{aligned} \tag{5}$$

Here ΔT_1 is the temperature difference at the high temperature end of two fluids, and ΔT_2 is that at the low temperature end.

4.1.4. Uncertainties

Uncertainties of measured parameters are analysed using the method introduced by Moffat [25]. The flowrate is measured by

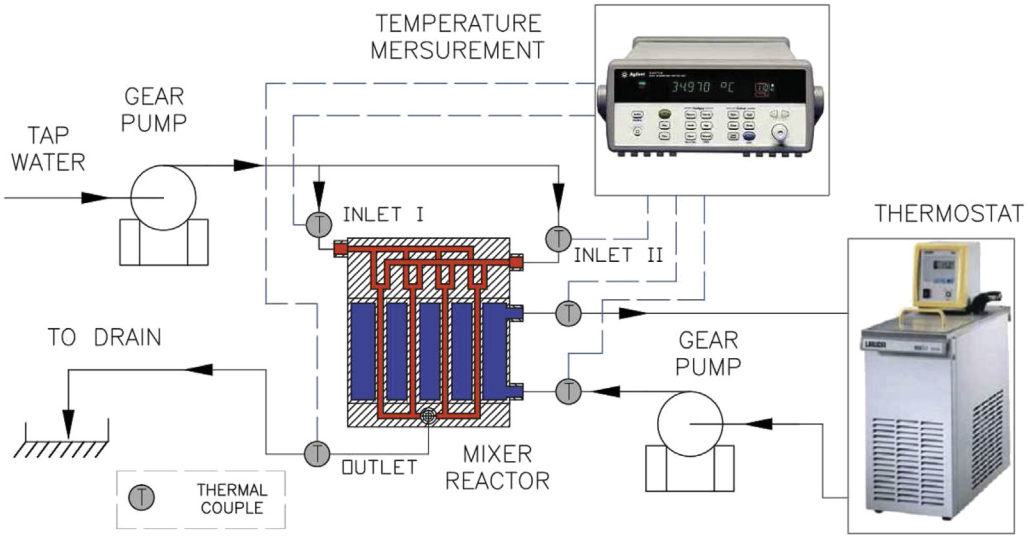

Fig. 8. Schema of the experimental system established for heat exchange tests.

weighting method where two sources of uncertainty happen: weight measurement and time counting. We use a precise digital balance whose uncertainty could be omitted (±0.1 g precision within max. 4200 g). A stopwatch is used for time measurement. For each measurement the time interval is more than 100 s with human error under ±0.5 s. Thus we have an uncertainty of flowrate measurement within ±0.5%. Uncertainty of temperature measurement, using in-house calibrated thermalcouples, is less than ±0.5 °C. Temperature difference then has a maximum error of ±1 °C. The temperature difference for heating test is around 25 °C and that of cooling test is 15 °C. Instrumental error for heat transfer rate, according to Equation (2), is calculated to be ±6.7% for cooling test and ±4.0% for heating test. If integrating the heat loss (10% max. before averaging), overall uncertainty for heat exchange rate is ±11.7% and ±9.0%. The same values of uncertainties are estimated for global heat transfer coefficient by experiment. For clarity, the uncertainties are shown as error-bars in reported figures.

4.2. Correlation calculation

Overall heat exchange coefficient, supposing fully developed flow at both channel-side and shell-side, could be estimated by considering this exchanger as two-stream shell-and-tube configuration. Estimation of overall heat transfer coefficient is based on three thermal resistances including tube-side convective resistance, heat conductive resistance through the tube wall and, shell-side convective resistance. Calculation is shown in Equations (6)–(9).

$$U_{\text{correlation}} = \frac{1}{\frac{d_o}{h_i d_i} + \frac{d_o}{2\lambda_{cc}} \ln\frac{d_o}{d_i} + \frac{1}{h_o}} \tag{6}$$

where d_i and d_o are internal and external diameters of parallel channels, respectively.

(i) Tube-side heat transfer coefficient:

For tube-side heat transfer coefficient under laminar flow, we use Sieder–Tate correlation [26]:

$$\frac{h_i d_i}{\lambda_{f,i}} = Nu_i = 1.86\left(Re_i Pr_{f,i}\frac{d_i}{l}\right)^{1/3}\left(\frac{\mu_{f,i}}{\mu_{w,i}}\right)^{0.14} \tag{7}$$

Moreover, tubes are supposed to have the same temperature along the wall. Most parameters are under reference temperature of average fluid temperature (indices f,i), while some are referred to the wall temperature of tubes under indices w,i; More conditions to use the Sieder–Tate correlation are shown in Equation (8).

$$\begin{aligned} Pr_{f,i} &= 0.48 - -16,700 \\ \frac{\mu_{f,i}}{\mu_{w,i}} &= 0.0044 - -9.75 \\ \left(Re_i Pr_{f,i}\frac{d_i}{l}\right)^{1/3}\left(\frac{\mu_{f,i}}{\mu_{w,i}}\right)^{0.14} &\geq 2 \end{aligned} \tag{8}$$

(ii) Conductive heat transfer coefficient

For heat conduction through the wall of tubes, thermal conductivity of Cobalt Chrome (at 20 °C) $\lambda_{cc} = 11$ W m^{-1} °C^{-1} is used.

(iii) Shell-side heat transfer coefficient

Shell-side calculation is based on KERN method, which is a simplified model to evaluate the performance of shell-and-tube heat exchangers. Correlation of Nusselt number of shell side is given by Equation (9).

$$\frac{h_o d_e}{\lambda_{f,o}} = Nu_o = j_h Re_o Pr_{f,o}^{1/3}\left(\frac{\mu_{f,o}}{\mu_{w,o}}\right)^{0.14} \tag{9}$$

Here, indices f,o means that the reference temperature is the average fluid temperature at the shell side; w,o means reference temperature being the wall temperature at outside of tube; j_h is shell-side heat transfer factor, which is related with Reynolds number and can be determined by diagram; d_e is the equivalent hydraulic diameter for shell side, and it can be calculated by parameters of tube diameter (outside) and pitch distance for square arrangement. More details on the use of KERN method can be found on the book “Chemical Engineering Design” by Sinnott [23].

The solving procedure of KERN model is based on heat transfer equations (conduction, tube-side convective and shell-side convective transfers) shown in Equation (10).

$$\begin{aligned} &\text{tube-side convection}: && \Phi_{\text{tube}} = h_i\frac{d_i}{d_o}(T_{w,i} - T_t)A_o \\ &\text{conduction}: && \Phi_{\text{conduct}} = \frac{2\lambda_{cc}}{d_o \ln\frac{d_o}{d_i}}(T_{w,o} - T_{w,i})A_o \\ &\text{shell-side convection}: && \Phi_{\text{shell}} = h_o(T_s - T_{w,o})A_o \end{aligned} \tag{10}$$

Here, convection heat transfer coefficients of shell-side (h_o) and tube-side (h_i) are in function of temperatures including tube-side fluid temperature (T_t), shell-side fluid temperature (T_s), inner channel temperature ($T_{w,i}$) and outer wall temperature ($T_{w,o}$).

To solve the equations, iterative computing is used. By approaching the values of $T_{w,i}$ and $T_{w,o}$, values of heat transfer rate (Φ_{tube}, Φ_{conduct}, Φ_{shell}) are compared until being identical. Firstly the three equations are combined to solve two unknown temperature values on inner wall $T_{w,i}$ and outer wall $T_{w,o}$. Then two heat convection coefficients (h_i and h_o) are calculated with known flow properties and fluid physical properties at reference temperature. Finally the overall heat exchange coefficient ($U_{\text{correlation}}$) is obtained combining three heat transfer coefficients and heat transfer rate.

4.3. Results of heat exchange study

4.3.1. Heat exchange rate

Shown in Fig. 9 are the heat exchange rates obtained under heating (a) and cooling (b) tests. Both measured results (experiment) and estimated results (KERN model) are presented.

Heat exchange rate is strongly related with fluid flowrate of both shell- and tube-side. From the experimental results in Fig. 9, heat exchange rates range from 80 to 171 W for the case of heating test (with the log-mean temperature difference being 23–28 °C), and 42–90 W for the case of cooling test (with the log-mean temperature difference being 14–16 °C). Increasing the utility fluid flowrate enhances the total heat flow thus provides better thermal control over the condition of process fluid.

According to the experiment, increasing the tube side flowrate also enhances heat exchange. When comparing the two cases of tube Reynolds numbers being 568 and 275, we observe higher heat transfer rate for the higher *Re* case. Under heating experiment, at least 20 W more heat flow happens at the higher *Re* case and under cooling experiment the difference is higher than 10 W.

The agreement between experimental and correlation results, however, seems to be far from satisfactory. The heat transfer rate of the tube-and-shell exchanger, calculated by KERN model, is under 31 W for heating test and 16 W for cooling test. These values are

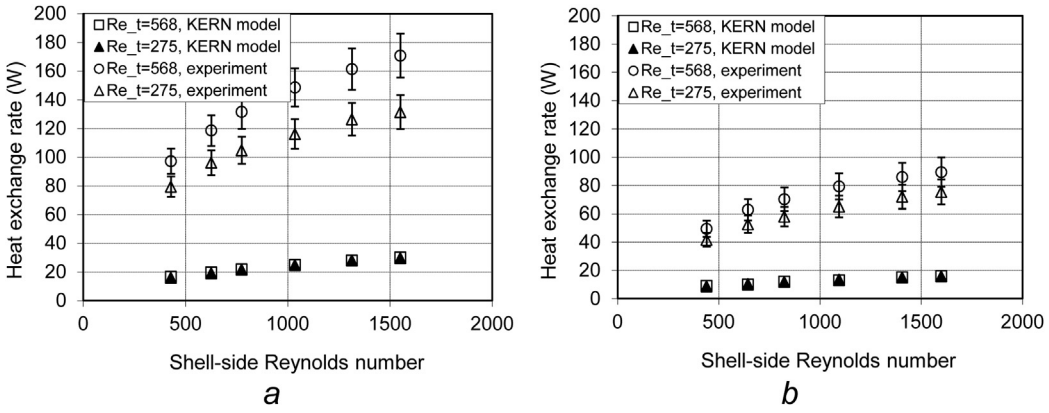

Fig. 9. Experimental and correlation-estimated heat exchange rate between utility fluid and process fluid versus Reynolds number (*Re*_t shows Reynolds number in tubes). (a) Heating test, for endothermic reaction usage; (b) cooling test, for exothermic reaction usage.

much smaller than experimental ones. For example, if considering the highest value of heat transfer rate for the heating test, a difference between 171 W and 31 W is found between experimental result and KERN model. Heat flow of 140 W happened inside the heat exchanger but not through the tube-and-shell structure.

4.3.2. End-effect heat exchange and non-established flow

The departure of the correlational result from that of experiment is supposed to be due to the difference between studied heat exchanger and a standard tube-and-shell configuration. Fig. 10 shows the overall heat exchange mechanism of studied heat exchanger.

Two reasons may explain the difference: end effect and transitional flow.

Firstly, a big portion of heat flow (Φ_r) should have taken place between the tube-side fluid and the heat exchanger itself, and then to the utility fluid. At one end (shown in the upper part of the shell side in Fig. 10, Φ_r), heat transfer happens between the utility fluid and the heat exchanger body. With the metal-made structure, a good thermal conductivity makes little temperature difference between the distribution channels and the upper wall of utility fluid chamber. At the other end (shown in lower part of the shell side in Fig. 10, Φ_r), heat transfers again from process fluid to utility fluid through the collector surface. KERN correlation considers only the heat exchange between the tube- and shell-side, shown as the portion Φ_t in the figure; while experimental measured heat exchange consists of both Φ_t and Φ_r. This extra heat exchange is considered as *end-effect*.

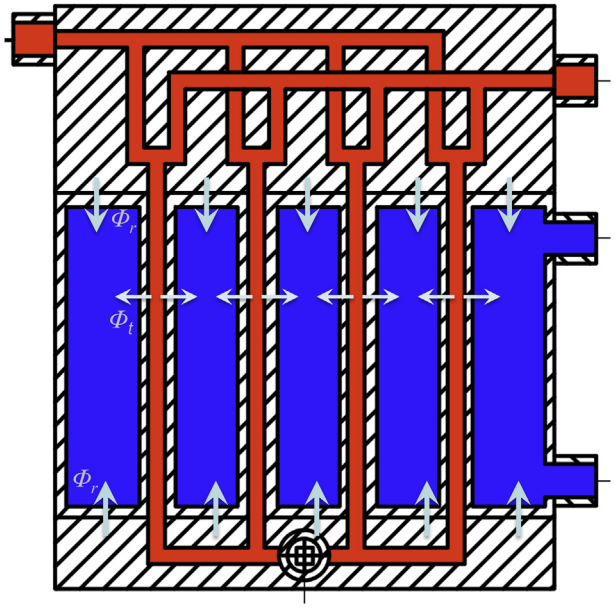

Fig. 10. Explanation of end-effect heat transfer (Φ_r) and tube-and-shell heat transfer (Φ_t) in overall heat exchange.

Secondly, both correlations at tube and shell side are based on developed flow which is hardly our case due to the geometry complexity. Fluid inside tubes are in transition regime (entrance flow) with more flow interactions than laminar flow – even with low *Re* numbers. The same transitional regime happens at shell side where secondary flow may take place. The transitory fluid movement at both sides may result in enhancement of heat convection, i.e. an underestimation of Φ_t by correlation.

The transfer surface considered in KERN model is the shell-side transfer surface A (where Φ_t happens); while in real case, both transfer surface of Φ_t and Φ_r should be considered. This explains why we introduce the effective surface $A_{effective}$.

4.3.3. Overall heat exchange coefficient

Overall heat exchange coefficients (U) under tested conditions are shown in Fig. 11. Values of experimental overall heat exchange coefficients vary around 2500–5000 W m^{-2} °C^{-1} for heating test, and around 2000–4000 W m^{-2} °C^{-1} for cooling test. The same trend between overall heat exchange coefficient and fluid flowrate is found as that of heat exchange rate. High flowrates of utility/process fluid result in high heat transfer coefficient.

Correlation-estimated values of heat exchange coefficient between shell- and tube-side, range only from 289 to 536 W m^{-2} °C^{-1}. As been already discussed, end effects contribute to overall heat exchange, with the correlation calculated heat exchange coefficient underestimated in addition.

4.4. Further discussions on heat exchange performance

4.4.1. Compactivity of heat exchanger

To show the *compactivity* of the studied heat exchanger, ratio of heat exchange capability and volume UA/V has been estimated. The value of UA/V is found to be around 200 kW m^{-3} °C^{-1}, which is relatively high compared with the value of 10 kW m^{-3} °C^{-1} for traditional tank reactors [27]. Two possible reasons resulting in this high ratio are the overall heat exchange coefficient and the transfer area. In one case, high overall heat exchange coefficient compensates to the compactivity although the specific transfer area (when only tube-and-shell exchange area is considered) is relatively small. The other possible case is that considering both tube-and-shell

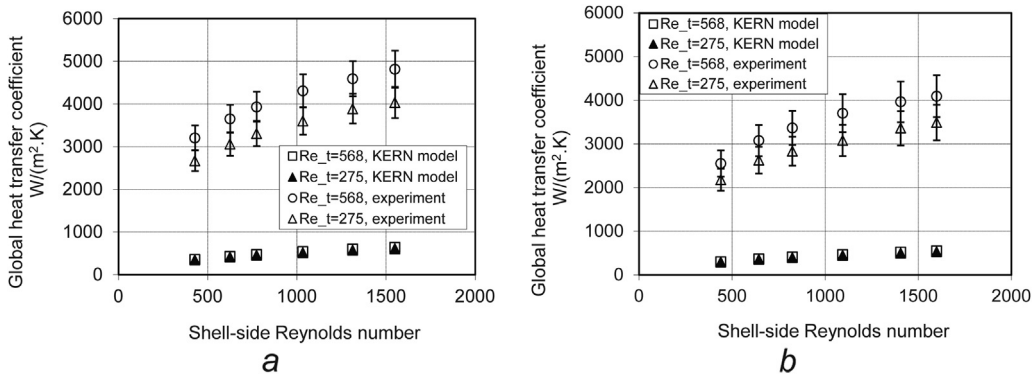

Fig. 11. Experimental and correlation-estimated global heat transfer coefficient versus Reynolds number (*Re*_t shows Reynolds number in tubes). (a) Heating test, for endothermic reaction usage; (b) cooling test, for exothermic reaction usage.

exchange area (1.26×10^{-3} m^2) and that of two end-effect transfer areas (1.46×10^{-3} m^2), the whole *effective* transfer area could be doubled. In this case the overall heat exchange coefficient initially calculated based on tube-and-shell exchange area is overestimated. Nevertheless, the high value of *UA*/*V* keeps being reliable since it is directly obtained from experimental analyses.

4.4.2. Shortage of exchange surface

The results also give out some clue on the design. Measured global heat transfer coefficient has been observed to be relatively high, since we have chosen a thermal conductive material and an appropriate reverse-flow type. However the heat exchange rate seems to be quite small, implying that the capability of this heat exchanger is limited facing certain highly exothermic reactions. Considering the heat transfer equation (4), a bigger transfer area is needed for future designs. Current effective specific transfer area *A*/*V* is 121 m^2 m^{-3} and it is not sufficient to be an intensified device compared with that summarised by Ref. [28]. Increasing the density of tube arrangement (more channels in parallel) could increase total transfer surface too. Otherwise, another way to increase the heat exchange rate is to expand the temperature difference, which is not only sometimes limited by processing conditions, but also being unfavourable from the viewpoint of the second law of thermodynamics [5].

5. Temperature control example – exothermic reaction

A fast, exothermic neutralisation reaction is used here as an application example. The aim is to study the thermal control ability of the multifunctional heat exchanger reactor, being applied in a continuous reaction combined with heat release.

5.1. Reaction principle

Sulphuric acid and sodium hydroxide solutions are mixed together for neutralization. The reaction is exothermic, with an enthalpy change of ΔH_r, kJ mol^{-1} (with molar amount of NaOH as the molar quantity reference). Basic reaction formula is shown in R1.

$$0.5H_2SO_4 + NaOH \rightarrow H_2O + 0.5Na_2SO_4 + \Delta H_r \quad (R1)$$

The reaction enthalpy is calculated from Hess's law:

$$\Delta H_r = 0.5\Delta H(Na_2SO_4) + \Delta H(H_2O) - 0.5\Delta H(H_2SO_4) - \Delta H(NaOH) \quad (11)$$

where, ΔH is the standard molar enthalpy of formation at the condition of 298.15 K and 1 bar, for each substances, kJ mol^{-1}; detailed substance properties are found from Ref. [29]. Value of the reaction enthalpy is then calculated as $\Delta H_r = -55.8$ kJ mol^{-1}.

The inorganic mineral producing reaction has a high kinetic rate which means that its an instantaneous reaction. The reaction time is much shorter than the fluid spatial time through the reactor. Reaction heat is released once two solutions are made in contact.

5.2. Calculation of temperature rise

The temperature rising character of studied reaction is calculated by energy conservation between reaction energy release and absorbed heat by process fluid (under adiabatic condition):

$$\Phi_{reaction} = \dot{m}c_p\Delta T_{adiabatic} = C_{NaOH}Q_{NaOH}\Delta H_r \quad (12)$$

where the index adiabatic means that the reaction is under adiabatic condition and all heat generation stays in the reaction product. In this case, the heat release from reaction is transferred to sensible heat in liquid, shown by a temperature rise. There is neither heat release to ambient (insulated from ambient) nor to the reactor (stable-state hypothesis). Heat capacity c_p of water is used during the calculation.

Different concentration pairs are employed for estimation, and finally a concentration pair of 0.5 mol L^{-1} for sulphuric acid and 1.0 mol L^{-1} for hydroxide sodium is chosen. Corresponding temperature rise is 6.6 °C. The concentration pair is used in the continuous reaction experiment.

5.3. Continuous reaction test

Solutions of acid and base are injected at an equal volume flowrate proportion inside the studied exchanger-reactor. The scheme of experiment is similar to that of heat exchange test shown in Fig. 8, except that two pumps are employed this time to deliver the two solutions separately into Inlet I and Inlet II. At the "utility fluid" side, coolant water is circulated with its inlet temperature being controlled by the thermostat bath at 6.0 °C.

Inlet/outlet temperatures of both coolant side and reaction side are recorded with thermocouples. Temperature rise of reaction side is calculated by the difference between the outlet (raised temperature by reaction enthalpy, ΔH_r) and inlet solutions (ambient temperature, 24.0 °C). Throughput of reaction (solution 1 and 2) is fixed at 3.3 mL s^{-1} (200 mL min^{-1}), while several flowrates of coolant, adjusted by the pumping system, are tested.

5.4. Temperature control effect in steady state

Fig. 12 shows temperature rise of reaction fluid under different cooling conditions by using proposed heat exchanger-reactor.

Firstly, at zero coolant flowrate, i.e. under adiabatic condition, measured temperature rise is 5.8 °C. Considering some inevitable heat loss to the ambient due to insufficient insulation, the experimental temperature rise corresponds well with the calculated value of 6.6 °C. The chosen exothermic reaction and concentration pair are satisfactory from this point of view.

Then by adjusting different coolant flowrates, the temperature rise is controllable through current heat exchanger-reactor. Instead of 5.8 °C under adiabatic condition, temperature rise is controlled at 3.2 °C by coolant water at flowrate of 1.7 mL s^{-1} (100 mL min^{-1}). By increasing the coolant flowrate, temperature rise becomes lower. At a coolant flowrate of 6.9 mL s^{-1} (417 mL min^{-1}), there is no more temperature difference of the process fluid between the outlet and inlet of reactor – meaning that the total heat release from reaction is evacuated by coolant fluid.

Finally, several other factors are adjustable in order to adapt with different reactions. Currently a temperature rise of 5.8 °C is verified to be controlled by cooling water that has an inlet temperature of 6.0 °C. Higher exothermic reactions, e.g. in case of more concentrated solutions, isothermal condition is expected to be still realizable by increasing coolant flowrate, reducing coolant inlet temperature, or prolonging the heat exchange channel.

5.5. Temperature evolution in transient state

To examine the transient behaviour of the exothermal reaction, Infrared camera (model SC7200, FLIR) is used to visualise the surface temperature evolution at the outside of studied reactor M1. During the measurement, insulation layers are removed so that the metal surface could be exposed directly to the camera.

Successive temperature profile photos are taken and some of them are shown in Fig. 13, along with the measurements of temperature at reactor outlet by thermocouple. Although the IR measurements are rather qualitative, the temperature evolution at external surface of reactor could be clearly observed. At the beginning of the graph, reaction didnt begin until the circulation of two solutions. The whole reactor is homogeneous in temperature as shown in the 1st photo. Once the reaction begins, colour of the upper side of the reactor changes from green to red, indicating a temperature rise of the collector part (shown at the upper side of photos 2 and 3); this high temperature zone extends until the whole reactor being heated, as shown in the 4th photo; finally, coolant fluid is circulated so that the temperature of reactor is cooled down (shown in the 5th photo).

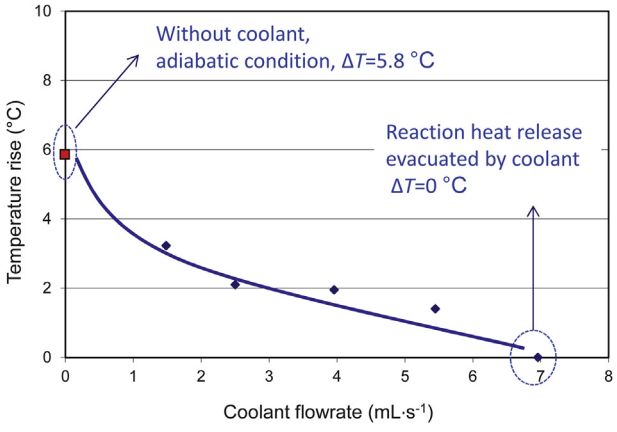

Fig. 12. Experimental temperature control effect over an exothermic reaction by studied heat exchanger-reactor.

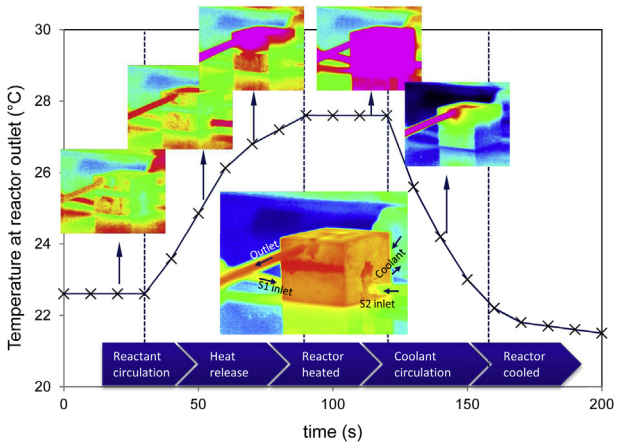

Fig. 13. Transitory temperature control effect over an exothermic reaction by studied heat exchanger-reactor (photo in the centre shows circulation arrangement of the reactor).

We notice that the collector part (in upper side of the photos) is heated earlier in the beginning of reaction. In our previous study [17], we have observed that the mixing takes place mainly in the collector part. Since a chemical reaction could not happen until two fluids are sufficiently in contact (insufficient mixing happens inside parallel channels), reaction heat could not be released until the two solutions passing through the collector. This temperature profile visualization hence verifies the mixing localization study.

Regarding the transient character, studied reactor has rapid responses under studied conditions. It takes firstly about 60 s from the beginning of reaction until the whole reactor being heated. Then the outlet temperature decreases as soon as the circulation of coolant begins. Finally within another 45 s, the outlet product temperature is controlled at an identical temperature as the initial one.

The fast exothermic reaction shows the capability of thermal condition control by using studied heat exchanger-reactor.

5.6. Verification of heat exchange compactness

With the isothermal point from steady state reaction test, heat exchange performance could be verified. At the coolant flowrate of 6.9 mL s^{-1} (417 mL min^{-1}), an energy conservation equation could be established between the utility fluid side and the coolant side. When inlet temperature and outlet one equals at the utility fluid side, total thermal energy release from exothermic reaction is evacuated by cooling fluid. Thus we have:

$$\Phi_{\text{reaction}} = \dot{m}c_{\text{p}}\Delta T_{\text{adiabatic}} = UA\Delta T_{\text{LMTD}} \tag{13}$$

With ΔT_{LMTD} the average temperature difference calculated by inlet and outlet temperatures of both sides (similar to that of heat exchange test). Here the value is 16.5 °C.

The compactivity of heat exchanger, UA/V, can be expressed as:

$$UA/V = \frac{\Phi_{\text{reaction}}}{\Delta T_{\text{LMTD}} V} \tag{14}$$

Here, reaction heat could be calculated by multiplying solution concentration (C, mol L^{-1}), flowrate (Q, m^3 s^{-1}) and reaction enthalpy (ΔH_{r}, kJ mol^{-1}).

Using equations (13) and (14), without getting into confusion of the surface area value (either tube-and-shell area or the effective exchange area), the compactivity of exchanger reactor is calculated as 218 kW m^{-3} $°C^{-1}$. This value is a verification of that obtained from heat exchange test around 200 kW m^{-3} $°C^{-1}$.

5.7. Discussions on reactor application

When using the exchanger-reactor for thermal related reactions, some special aspects need to be considered. Total heat generation (thermal load for coolant) of an exothermic reaction increases proportionally with the molar flowrate of process fluid. Without modifications to concentration, reaction under high flowrate at process fluid side requires more heat flow for thermal condition management. Simply increasing the volumetric flowrate of process fluid with the aim of enhancing thermal control is not enough in that case, since more thermochemical energy will be produced. Increasing the volumetric flowrate and at the same time controlling the molar flowrate of reactants within chemical constraints (appropriate residence time, concentration, etc.) are the keys for better thermal management.

Raising the flowrate of utility fluid at the shell side, however, always favours thermal condition control during an exothermic reaction. Since the study on total pressure drop characters indicates that the pressure drop at the shell side is relatively small, techniques such as adding micro-fins [30] to the external surface of tubes, or adding baffles [31] to shell side may be considered to further enhance the heat transfer.

6. Conclusions and perspectives

A multichannel heat exchanger-reactor with arborescent structure is designed, fabricated and tested. Firstly, flow distribution uniformity is investigated both quantitatively by CFD simulation and qualitatively by optical tracer visualization. Then, heat exchange performance of this heat exchanger-reactor has been experimentally investigated. An estimation of heat exchange between shell and tube side is implemented by employing established correlations, including KERN method to the shell side. Finally an exothermic reaction is used to assess the capability of thermal condition control of studied exchanger-reactor.

CFD results show that under studied conditions, the proposed arborescent structure provides almost uniform distributing feature among channels. Maximum deviation of flowrate with respect to the mean value (D_{ch}) is under 10% for the 16 channels. Flow visualization by optical tracer and fast camera also confirms qualitatively the distribution uniformity. Numbering-up of multiple channels in application of processing equipment can be realized in similar manner.

From the heat exchange test, high overall heat exchange coefficients around 2000–5000 W m^{-2} $°C^{-1}$ are obtained. By comparing experimental results with correlational estimations, it is observed that an important portion of heat transfer is found through the two ends of the heat exchanger via distributors and collector. Another reason is that non-established flow in both tube and shell side enhance convective heat transfer.

Heat exchange compactivity, the ratio UA/V, is tested and verified to be at the level of 200 kW m^{-3} $°C^{-1}$, which is 20 times higher than traditional tank reactors. This parameter shows the compact feature of studied heat exchanger. Concerning surface-to-volume ratio A/V, current value of 121 m^2 m^{-3} is lower than other intensified designs. Benefit of low A/V ratio but high UA/V ratio is that hydraulic friction factor between wall and fluid is minor, but without deteriorating overall heat exchange performance. High throughput at both process and utility side is possible thanks to low pressure drop.

The rapid exothermic reaction test shows that compared with a temperature rise of 5.8 °C under adiabatic reaction condition, isothermal condition is achievable by circulating certain flowrate of coolant. Thermal condition is thus successfully manipulated experimentally using studied heat exchanger-reactor.

Our future works are intended at the structural optimisation of similar heat exchanger-reactor. Several directions are proposed, as detailed below.

Firstly, constructal optimized tree-like structures can be used instead of “non-optimized” distributors and collector in this study. Further structural improvement can be realised by a cellular automaton based algorithm [22] regarding both uniform flow distribution and minimum pressure drop.

Secondly, another study concerning possible application of residence time distribution on multichannel systems has been done and will be reported in our future paper. Modular, varied channel length concepts will be considered for flexible residence time utilization.

Finally, a second law analysis of the multifunctional device is also expected by proposing a pertinent criterion that accounts for the pressure loss, the heat transfer and mixing (chemical reaction) performances.

Acknowledgements

This work is partially financed by the French ‘Agence Nationale de la Recherche’ (_501100001665) within the project MIGALI (ANR-09-BLAN-0381-2). Authors would address their thanks to French Ministère de l’Enseignement Supérieur et de la Recherche, for their financial support to the PhD study. Technical services from Thierry Goldin, Jonathan Outin and Cédric Poinard in LOCIE, Polytech Annecy-Chambéry are gratefully appreciated.

References

[1] Lee H, Saleh K, Hwang Y, Radermacher R. Optimization of novel heat exchanger design for the application to low temperature lift heat pump. Energy 2012;42:204–12.
[2] Zaversky F, Sánchez M, Astrain D. Object-oriented modeling for the transient response simulation of multi-pass shell-and-tube heat exchangers as applied in active indirect thermal energy storage systems for concentrated solar power. Energy 2014;65:647–64.
[3] Streiff F. De l’efficacité énergétique à la compétitivité économique. In: ADEME, Vous, editors. Agence de l’Environnement et de la Maîtrise de l’Energie; 2013.
[4] Walmsley MRW, Walmsley TG, Atkins MJ, Neale JR. Methods for improving heat exchanger area distribution and storage temperature selection in heat recovery loops. Energy 2013;55:15–22.
[5] Cheng X, Liang X. Optimization principles for two-stream heat exchangers and two-stream heat exchanger networks. Energy 2012;46:386–92.
[6] Cheng X. Entropy resistance minimization: an alternative method for heat exchanger analyses. Energy 2013;58:672–8.
[7] Brandner J, Bohn L, Henning T, Schygulla U, Schubert K. Microstructure heat exchanger applications in laboratory and industry. Heat Transf Eng 2007;28:761–71.
[8] Fan Y, Luo L. Recent applications of advances in microchannel heat exchangers and multi-scale design optimization. Heat Transf Eng 2008;29:461–74.
[9] Luo L. Heat & mass transfer intensification and shape optimization: a multi-scale approach. London: Springer; 2013, ISBN 978-1-4471-4741-1.
[10] Lalot S, Florent P, Lang SK, Bergles AE. Flow maldistribution in heat exchangers. Appl Therm Eng 1999;19:847–63.
[11] Tondeur D, Luo L. Design and scaling laws of ramified fluid distributors by the constructal approach. Chem Eng Sci 2004;59:1799–813.
[12] Fan Y, Boichot R, Goldin T, Luo L. Flow distribution property of the constructal distributor and heat transfer intensification in a mini heat exchanger. AIChE J 2008;54:2796–808.
[13] Luo L, Tondeur D, Le Gall H, Corbel S. Constructal approach and multi-scale components. Appl Therm Eng 2007;27:1708–14.
[14] Luo L, Fan Y, Zhang W, Yuan X, Midoux N. Integration of constructal distributors to a mini crossflow heat exchanger and their assembly configuration optimization. Chem Eng Sci 2007;62:3605–19.

[15] Fan Z, Zhou X, Luo L, Yuan W. Evaluation of the performance of a constructal mixer with the iodide-iodate reaction system. Chem Eng Process Process Intensif 2010;49:628–32.
[16] Luo L, Fan Y. Fluids circulation module. WO/2012/010620, 2012.
[17] Guo X, Fan Y, Luo L. Mixing performance assessment of a multi-channel mini heat exchanger reactor with arborescent distributor and collector. Chem Eng J 2013;227:116–27.
[18] Post S. Applied and computational fluid mechanics. Jones & Bartlett learning; 2010.
[19] Panić S, Loebbecke S, Tuercke T, Antes J, Bošković D. Experimental approaches to a better understanding of mixing performance of microfluidic devices. Chem Eng J 2004;101:409–19.
[20] Tondeur D, Fan Y, Luo L. Constructal optimization of arborescent structures with flow singularities. Chem Eng Sci 2009;64:3968–82.
[21] Wang L, Fan Y, Luo L. Heuristic optimality criterion algorithm for shape design of fluid flow. J Comput Phys 2010;229:8031–44.
[22] Wang L, Fan Y, Luo L. Lattice Boltzmann method for shape optimization of fluid distributor. Comput Fluids 2014;94:49–57.
[23] Sinnott RK. Chemical engineering design. In: Coulson and Richardson's chemical engineering. Oxford: Elsevier Butterworth-Heinemann; 2005.
[24] Kuppen T. Heat exchanger design handbook. Marcel Dekker, Inc.; 2000.
[25] Moffat RJ. Describing the uncertainties in experimental results. Exp Therm Fluid Sci 1988;1:3–17.
[26] Sieder EN, Tate GE. Heat transfer and pressure drop of liquids in tubes. Ind Eng Chem Res 1936;28:1429–35.
[27] Ferrouillat S, Tochon P, Peerhossaini H. Micromixing enhancement by turbulence: application to multifunctional heat exchangers. Chem Eng Process 2006;45:633–40.
[28] Anxionnaz Z, Cabassud M, Gourdon C, Tochon P. Heat exchanger/reactors (HEX reactors): concepts, technologies: state-of-the-art. Chem Eng Process Process Intensif 2008;47:2029–50.
[29] David J, Lide R. Standard thermodynamic properties of chemical substances. In: CRC handbook of chemistry and physics. Taylor & Francis Group; 2000.
[30] Pan M, Jamaliniya S, Smith R, Bulatov I, Gough M, Higley T, et al. New insights to implement heat transfer intensification for shell and tube heat exchangers. Energy 2013;57:208–21.
[31] Wang S, Wen J, Li Y. An experimental investigation of heat transfer enhancement for a shell-and-tube heat exchanger. Appl Therm Eng 2009;29:2433–8.